Multi-Modal 3D Image-Based Simulation of Hydrogen Embrittlement Crack Initiation in Al-Zn-Mg Alloy

Higa, Ryota
Graduate Course in Mechanical Engineering, Kyushu University

Fujihara, Hiro
Department of Mechanical Engineering, Kyushu University

Toda, Hiroyuki
Department of Mechanical Engineering, Kyushu University

Kobayashi, Masakazu
Department of Mechanical Engineering, Toyohashi University of Technology

他

出版情報：MATERIALS TRANSACTIONS. 65 (8), pp.899-906, 2024-08-01. Japan Institute of Metals
バージョン：

Materials Transactions, Vol. 65, No. 8 (2024) pp. 899 to 906

Multi-Modal 3D Image-Based Simulation of Hydrogen Embrittlement Crack Initiation in Al-Zn-Mg Alloy*[1]

Ryota Higa[1,*2], Hiro Fujihara[2], Hiroyuki Toda[2], Masakazu Kobayashi[3], Kenichi Ebihara[4] and Akihisa Takeuchi[5]

[1]*Graduate Course in Mechanical Engineering, Kyushu University, Fukuoka 819-0395, Japan*
[2]*Department of Mechanical Engineering, Kyushu University, Motooka, Fukuoka 819-0395, Japan*
[3]*Department of Mechanical Engineering, Toyohashi University of Technology, Toyohashi 444-8122, Japan*
[4]*Center for Computational Science & e-Systems, Japan Atomic Energy Agency, Naka-gun, Ibaraki 319-1195, Japan*
[5]*Japan Synchrotron Radiation Research Institute, Sayo-gun, Hyogo 679-5198, Japan*

In Al-Zn-Mg alloy, hydrogen (H) leads remarkably to the degradation of mechanical properties. It is indispensable to suppress this phenomenon called hydrogen embrittlement (HE) for developing the high-strength Al-Zn-Mg alloy. Because intergranular fracture (IGF) is mainly observed when HE occurs in the alloy, we need to understand the initiation behavior of IGF in order to suppress HE. Heterogeneous distribution of stress, strain and H concentration usually influence the IGF initiation in polycrystalline material. In the present study, we investigated distribution of stress, strain, and H concentration in actual fractured regions by simulation employing a crystal plasticity finite element method and H diffusion analysis in a 3D image-based model, which was created based on 3D polycrystalline microstructure data obtained from X-ray imaging technique. Combining the simulation and *in-situ* observation of the tensile test sample by X-ray CT, we examined the distribution of stress, strain, and H concentration in actual crack initiation behavior. Based on this, the condition for intergranular crack initiation were discussed. As a result, it is revealed that stress normal to grain boundary induced by crystal plasticity dominates intergranular crack initiation. In contrast, accumulation of internal H due to the stress has little impact on crack initiation.
[doi:10.2320/matertrans.MT-L2024007]

(Received April 2, 2024; Accepted May 7, 2024; Published May 31, 2024)

Keywords: *Al-Zn-Mg alloy, hydrogen embrittlement, crack initiation, crystal plasticity finite element method, hydrogen diffusion analysis*

1. Introduction

Al-Zn-Mg alloy exhibits excellent specific strength and is used as a structure material for aircraft and bullet trains. It is known that the strength of Al-Zn-Mg alloy increases with the addition of more Zn and/or Mg [1, 2]. However, the susceptibility to stress corrosion cracking (SCC) increases at the same time [3] and makes it unusable as a practical alloy. Overcoming hydrogen embrittlement (HE) is necessary to achieve both high strength and practicality in Al-Zn-Mg alloys, which is the main cause of SCC [4, 5].

HE fracture of Al-Zn-Mg alloys is characterized by crack initiation at grain boundaries (GB) [6–8]. The fracture at GB can be understood through the mechanism of H-enhanced decohesion (HEDE) [9]. In the mechanism, weakening the atomic bonding at GBs by H leads to fracture. This mechanism has been evaluated by first-principles calculations. For example, Yamaguchi *et al.* have computationally shown that the cohesive energy at GBs decreases as the H concentration on GBs increases [10]. Moreover, they reported that spontaneous debonding at GB occurs when the H concentration reaches 20 atom/nm^2. However, it is unclear whether such H concentration is realized or not at actual situation. Thus, the initiation of intergranular cracks in aluminum alloys is not understood completely at present. By the way, the H accumulation is caused by stress localization which results from the mismatch in deformation due to differences in the slip system among grains in the deformed polycrystalline metal. Therefore, it is necessary for explaining H enrichment at GBs to estimate the interaction between grains.

Since experimental direct evaluation of such behavior is difficult, the numerical simulation can be used. For example, Miresmaeili *et al.* used a coupled crystal plasticity finite element method (CPFEM) and H diffusion analysis to calculate H concentration behavior associated with stress localization. The results show that H accumulate around a specific GB as the hydrostatic stress increases [11]. However, this method also has problems. Most studies that calculate H concentration by simulation use a grain model randomly generated on a computer, which often simplifies the complex morphology of grains. In such cases, the stress concentration caused by the complex grain morphology is ignored, resulting in underestimation of stress and H concentration. Therefore, there is a large error between the simulation results and the actual stress and H concentration in the material.

Image-based two-dimensional (2D) grain models are often used to account for the effects of complex grain structures in practical alloys. This method involves imaging the grain structure on the surface of a specimen and modeling the resulting 2D grain image as it is. Some researchers have applied this method to the analysis of crack initiation behavior. For example, Arora *et al.* simulated stress distribution using a 2D image-based model and compared the stress distribution with crack initiation behavior [12]. As a result, they reported that intergranular cracks tend to occur at GB with high hydrostatic stress. This is considered to be due to H enrichment at GB with high hydrostatic stress, which causes intergranular crack initiation by the HEDE mechanism. Pouillier *et al.* also calculated the stress distribution in

*[1]This Paper was Originally Published in Japanese in J. JILM **73** (2023) 530–536. Abstract was slightly modified.
*[2]Corresponding author, E-mail: higa.ryota.817@s.kyushu-u.ac.jp

Al-5%Mg using a similar method and reported that cracking occurs at GB where the vertical stress exceeds 170 MPa [13]. However, the 2D simulation ignores the effect of grain structure in the thickness direction [14], thus hindering precise reproduction of the actual stress localization behavior.

To solve this problem, a three-dimensional (3D) image-based model is necessary. A combination of serial sectioning and EBSD observation [15] is known as a method to realize such an image-based model. However, the calculated specimen behavior cannot be experimentally evaluated since serial sectioning is a method that destroys the specimen.

We focused on the possibility of performing both experimental and simulation evaluations on the same specimen by modeling using diffraction contrast tomography (DCT) [16]. It is a nondestructive method for obtaining high-resolution 3D grain images. Therefore, after imaging 3D grain structure, the specimen can be subjected to tensile test to observe crack initiation behavior. This enables direct comparison of the crack initiation behavior with the results of simulation using the 3D image-based model. In this study, a multi-modal 3D simulation coupled with CPFEM and H diffusion analysis is performed using the 3D image-based model. The objective of this study is to accurately calculate the stress localization and H concentration behavior induced by complex 3D grain structure and to clarify the effect of crystal plasticity on intergranular crack initiation.

2. Experimental Methods

2.1 Material

Al-Zn-Mg alloy (8.4 mass% Zn, 0.99 mass% Mg) was used in the present study. The process of preparing the specimens is as follows. After casting, the specimens were homogenized (773 K-2 h) and hot rolled (723 K) at a reduction ratio of 95%. After hot rolling, the final plate thickness was 0.6 mm. After rolling, solution treatment (773 K-2 h) was performed, followed by rapid cooling in ice water. Aging treatment (393 K-40 h + 453 K-7 h) was started immediately in an oil bath. The first aging treatment (393 K-40 h) brought the specimens to the peak aging state, and the second aging treatment (453 K-7 h) brought them to the over-aged state. During casting, the molten metal was stirred with an iron rod to add a small amount of iron in order to increase the volume fraction of particles. X-ray CT images at no loading revealed that the volume fraction of particles was increased to 0.12% by the addition of iron. The particles in the alloy were extracted using the thermal phenol method, and quantitative analysis by SEM-EDX showed that the average composition of the particles was $Al_{79}Fe_{14}Zn_7$. The linear absorption coefficient of the particles was estimated from the X-ray CT image, and the density was calculated using this value to be 5.4 g/cm^3. Assuming that all of the added iron was used to form the particles, the amount of iron added was estimated from the volume fraction of the particles, average composition, and density to be 0.058 mass%.

The reasons for selecting the composition and aging conditions of the specimens are provided below. Fujihara *et al.* conducted tensile tests using materials with the same composition and aging conditions as in the present study [17]. They observed the fracture surface of the specimen after fracture and confirmed the existence of intergranular fracture surface (fracture area of fracture surface: 36%) and quasi-cleavage fracture surface (fracture area of fracture surface: 31%) on the fracture surface. Shimizu *et al.* conducted tensile tests of H-charged specimens (H concentration: 2.15 mass ppm) and specimens with reduced H concentration (H concentration: 0.41 mass ppm) using materials with similar compositions (Al-10.1%Zn-1.2%Mg) and aging conditions to those used in the present study [18]. They reported that the ductility of the H-charged specimens was inferior to that of the specimens with reduced H content. Therefore, the brittle fracture observed by Fujihara *et al.* is considered to be due to HE. For these reasons, the composition and aging conditions of the specimens in this study are considered to be sufficiently affected by HE. Therefore, it was judged that the specimens were suitable for the analysis of crack initiation behavior. Moreover, Shimizu *et al.* conducted tensile tests on H charged specimens (H concentration: 11.8 mass ppm) using a material with a similar composition (Al-9.6%Zn-1.8%Mg) to that used in the present study at the peak aging state [19]. The authors reported that the specimens fractured immediately after reaching the elastic limit with almost no plastic deformation. Therefore, we concluded that it would be difficult to observe crack initiation behavior in the peak aging state of the specimens in this study. For these reasons, the composition and aging conditions of the specimens were selected.

Tensile specimens were cut using an electrical discharge machine (EDM) in the same geometry as in the previous literature [20] so that the tensile direction of the specimen was parallel to the rolling direction of the plate. In addition, EDM was performed in water in order to charge the specimens with H. The H content in the specimen after EDM was measured by thermal desorption analysis (TDA) and that was 7.0 mass ppm. Since H was concentrated on the specimen surface immediately after EDM, the specimen was kept at room temperature for 4 days after EDM to distribute H throughout the interior of the specimen. The diffusion distance L was estimated to be about 1.9 mm over the 4 days using the effective diffusion coefficient of 7050 alloy ($D_{H,eff} = 1.1 \times 10^{-11}$ m^2/s) [21] as reported by Young *et al.* The value of 4 days is sufficiently longer than the thickness of the specimen (0.6 mm).

2.2 DCT

The 3D grain structure of the specimen gauge area was acquired by DCT. This observation was performed at the beamline BL20XU of SPring-8, a high-brilliance synchrotron radiation facility. An X-ray beam with an energy of 30 keV and monochromatized by a double-crystal monochromator using Si(111) planes was used for the imaging. A CMOS camera with a pixel size of 3.13 μm and 2048 × 2048 pixels was positioned 6 mm behind the specimen to acquire diffraction spots from the (111), (200), and (220) lattice planes of aluminum. The specimen was mounted on a high-precision rotation stage, and 3600 diffraction images were acquired while the specimen was rotated 360°. Using the diffraction spots obtained, the crystal orientation of all the grains in the specimen gauge area was obtained, and a 3D grain image was reconstructed.

2.3 Tensile test and *in-situ* X-ray CT

The same specimen was subjected to the tensile test, and the crack initiation behavior was observed by X-ray CT. This observation was also performed at the BL20XU. During the tensile test, imaging was performed at unloading, immediately after yielding, and thereafter every 0.02 mm displacement. A displacement holding time of 10 min was set during each imaging step. The applied strains of the specimen gauge area during imaging were 0.0, 0.97, 3.2, 5.6, 9.2, 13.4, 19.3, and 23.5%. In the imaging, the X-ray energy was set to 20 keV and the X-ray beam was monochromatized by a double-crystal monochromator using Si(111) planes. The detector consists of a CMOS camera with a pixel size of 0.477 µm and 4000 × 2624 pixels, a single-crystal LuAG scintillator, and a 20-fold optical lens. The specimen was mounted on a high-precision rotation stage, and 1800 X-ray transmission images were acquired while the specimen was rotated 180°. The distance from the specimen to the detector was 20 mm. From these transmitted images, a 3D image of the specimen was reconstructed by the convolution back projection method [22].

2.4 CPFEM and H diffusion analysis

The general finite element method software ABAQUS incorporating the crystal plasticity subroutine developed by Huang [23] was used in CPFEM. The constitutive equations used in this study are as follows. First, the velocity gradient $\boldsymbol{L}$ of the deformation decomposed into an elastic part $\boldsymbol{L}_e$ and a plastic part $\boldsymbol{L}_p$.

$$\boldsymbol{L} = \boldsymbol{L}_e + \boldsymbol{L}_p \tag{1}$$

$\boldsymbol{L}_e$ can be calculated by the linear relationship between stress and strain. $\boldsymbol{L}_p$ is defined by the following formula.

$$\boldsymbol{L}_p = \sum_{\alpha=1}^{n} \dot{\gamma}^{(\alpha)} (\boldsymbol{m}^{(\alpha)} \otimes \boldsymbol{n}^{(\alpha)}) \tag{2}$$

$\dot{\gamma}^{(\alpha)}$ is the slip rate on the slip system α, and $\boldsymbol{m}^{(\alpha)}$ and $\boldsymbol{n}^{(\alpha)}$ are vectors representing the slip direction and normal to slip plane, respectively. $\dot{\gamma}^{(\alpha)}$ is defined by the power law visco-plastic approximation formula [24–26].

$$\dot{\gamma}^{(\alpha)} = \dot{\alpha}^{(\alpha)} \left[\frac{\tau^{(\alpha)}}{g^{(\alpha)}}\right] \left|\frac{\tau^{(\alpha)}}{g^{(\alpha)}}\right|^{n-1} \tag{3}$$

$\dot{\alpha}^{(\alpha)}$ is the reference value of the slip rate on the slip system α, and $\tau^{(\alpha)}$ is the resolved shear stress, and $g^{(\alpha)}$ is the slip resistance, and n is the rate sensitivity exponent. The temporal gradient of $g^{(\alpha)}$ is defined by the following formula assuming that deformation behavior follows the latent hardening law [27].

$$\dot{g}^{(\alpha)} = \sum_{\beta=1}^{n} h_{\alpha\beta} |\dot{\gamma}^{\beta}| \tag{4}$$

$h_{\alpha\beta}$ is the hardening matrix that represents the interaction between slip system α and β. It is called the self-hardening coefficient when $\alpha = \beta$ and the latent hardening coefficient when $\alpha \neq \beta$. The self-hardening coefficient represents the effect of slip system α alone, unaffected by other slip systems, and is defined by the following formula.

$$h_{\alpha\alpha} = h_0 \,\mathrm{sech}^2 \left|\frac{h_0 \gamma}{\tau_s - \tau_0}\right| \tag{5}$$

Here, h_0 is the initial hardening module, and τ_s is the saturated shear yield stress, and τ_0 is the initial shear stress. On the other hands, the latent hardening coefficient is defined by following formula.

$$h_{\alpha\beta} = q h(\gamma) \tag{6}$$

The constant q represents the ratio of self-hardening to latent hardening. In the present study, it is assumed that $q = 1$ and the hardening is equal in all slip systems. By the way, Fujihara *et al.* performed CPFEM using the material with the same composition and aging conditions as in the present study [17]. There, the parameters used in CPFEM were optimized by comparing stress-strain curve obtained from tensile tests with those obtained from CPFEM. The parameters optimized by Fujihara *et al.* was used in eqs. (2)–(6). In CPFEM, nodal solutions are obtained by extrapolating from the values of the integral points of the elements to which they belong, and calculation is done grain by grain. Therefore, nodes on the GB and the GB triple line have multiple nodal solutions. In the study, the average value of multiple nodal solutions was used as the calculated value at that nodal in order to uniquely determine stress and strain on GB.

In H diffusion analysis, Oriani's local equilibrium model [28] was used. In the model adopted in the study, H diffusion formula is defined as follows considering H diffusion due to the gradient of hydrostatic stress $\nabla\sigma_h$.

$$\frac{\partial C_H}{\partial t} = D_{H,eff} \nabla^2 C_H - \nabla \cdot \left(\frac{D_{H,eff} C_H \bar{V}_H}{RT} \nabla\sigma_h\right) \tag{7}$$

$D_{H,eff}$ is the effective diffusion coefficient, which that includes the effect of H trapping and detrapping, and we used the value of 7050 alloy presented by Young *et al.* ($D_{H,eff} = 1.1 \times 10^{-11}\,m^2/s$) [21]. C_H is the total H concentration in the interstitial and trap sites. $\bar{V}_H$ is the partial molar volume, and R is the gas constant, and T is the absolute temperature. The initial condition is that C_H, which is the total H concentration in the specimen minus the molecular H content in the pores C_{H_2}, is constant throughout the specimen. C_{H_2} was defined by the following equation [29].

$$C_{H_2} = 2N_A \frac{4\gamma V_{pore}}{d_{pore} RT} \tag{8}$$

Here, N_A is the Avogadro constant, and γ is the surface energy (1 J/m^2). d_{pore} and V_{pore} are the sphere equivalent diameter and volume of the pore respectively and were calculated from X-ray CT images at unloading. The total H concentration in the specimen was 7.0 mass ppm obtained by TDA, and 6.915 mass ppm, which was obtained by subtracting C_{H_2} from 7.0 mass ppm, was used as the initial state C_H.

The applied strain of the specimen gauge area was set to 0.97% in the crystal plasticity analysis. This value is the applied strain at one stage before the imaging stage when the initial crack occurred. In the H diffusion analysis, the diffusion behavior was calculated under the condition that the hydrostatic stress distribution at this loading strain was maintained for 10 min.

2.5 3D image-based model

The simulation model was made to reproduce the 3D grain

shape and orientation observed by DCT. Tetrahedral quadratic elements were used as the model components because they enable the creation of complex 3D models and guarantee the degree of freedom of the elements themselves. Since the number of elements becomes large and the calculation cost is high if a model that precisely reproduces all grains that exist in the specimen gauge area is created, the model was created by dividing it into two regions (regions B1 and B2), as shown below. In region B1, the model was fabricated to precisely reproduce the 3D shape of grains obtained by DCT using fine elements. The grains in the center of the specimen were selected to belong to region B1, and region B1 was set as the region of interest. In region B2, coarse elements were used to roughly reproduce the grain shape by meshing while ignoring the shape of GB. Moreover, in order to keep a distance between the grains in region B1 and the nodes that set the constraint conditions, a perfectly elastoplastic region A was created outside of the specimen gauge area to mimic the shape of the specimen in the area outside of the specimen gauge area.

In the finite element method, due to an element size dependence in the calculated values, if the element size is too large, the accuracy of the calculation cannot be guaranteed. Therefore, the element size dependence of the nodal solution was investigated, and the optimal element size was determined as follows. One GB in the region of interest was selected, and simulation models were created with element sizes of 2.5 μm, 5 μm, 10 μm, 20 μm and 40 μm within the two grains comprising the GB. Then, the averaged hydrostatic stress σ_h within the extracted GB was calculated using the CPFEM. The results were obtained as shown in Fig. 1. A second-order polynomial approximation curve is shown as a gray line in Fig. 1. The approximate curve shows that σ_h increases as the element size decreases, but σ_h converges around $a = 15$ μm. Therefore, an element size of 10 μm is considered sufficient. Thus, the element size at the GB on the surface was set to 10 μm, and the element size inside the specimen, where the stress gradient is expected to be smaller than on the surface, was set to 30 μm.

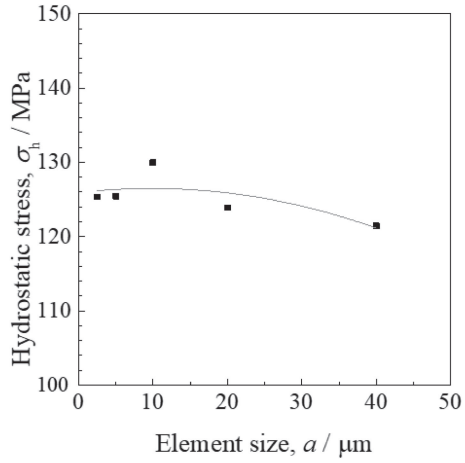

Fig. 1 Element size dependence of hydrostatic stress. The values are mean value of hydrostatic stress at each node in the GB. The gray line is approximate curve ($\sigma_h = 125.93078 + 0.11475 \times a - 0.00586 \times a^2$).

3. Results

3.1 Results of DCT and X-ray CT

Figure 2 shows the 3D grain image obtained by DCT at unloading. There were 155 grains in the specimen gauge area. The sphere equivalent of each grain was calculated using the 3D grain images and the mean value of all grains was found to be 1.6×10^2 μm. As a result of *in-situ* observation using X-ray CT, the crack was first observed at the applied strain of $\varepsilon_{appl} = 3.2\%$. The cracks image is shown in Fig. 3. Cracks initiated within the region of interest are numbered in the figure. A total of 13 cracks were observed from the GB and GB triple junction lines on the surface. For cracks 1∼7, which were initiated within the region of interest, the GB and GB triple lines where the cracks were initiated were identified by overlaying the X-ray CT images at the stage of $\varepsilon_{appl} = 3.2\%$ and the DCT images. Cracks 1∼4 initiated from the GB and cracks 5∼7 initiated from the GB triple lines. Because there were coarse pores in the vicinity of the initiation point of crack 7, crack 7 was excluded from the following analysis and the stress concentration for the crack can be caused by them rather than crystal plasticity. No coarse pores were observed in the vicinity of the cracks for cracks 1∼6.

3.2 Results of simulation

Figure 4 shows the 3D image-based model. The number of grains in region B1 is 68. Figure 5 shows the results of CPFEM and H diffusion analysis at $\varepsilon_{appl} = 0.97\%$. In Fig. 5, the simulation results are superimposed on the grain images in Fig. 2. It is observed that stress localization occurred on the GB due to the interaction between the grains, and H accumulation occurred in response to the localization of hydrostatic stress. As can be seen in Fig. 5, the degree of stress localization and H accumulation was not uniform across all GBs, and there were some GBs where the degree of

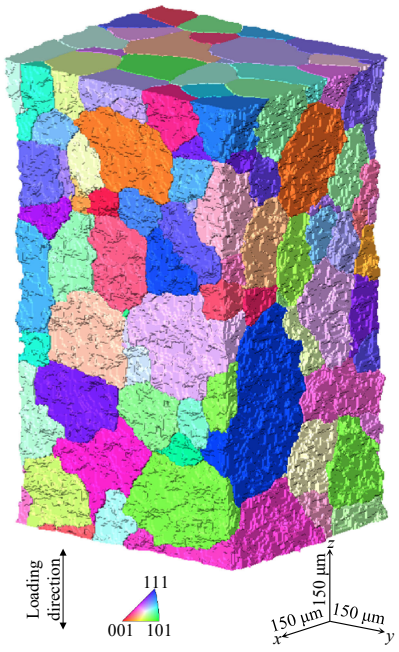

Fig. 2 3D grains and misorientations image.

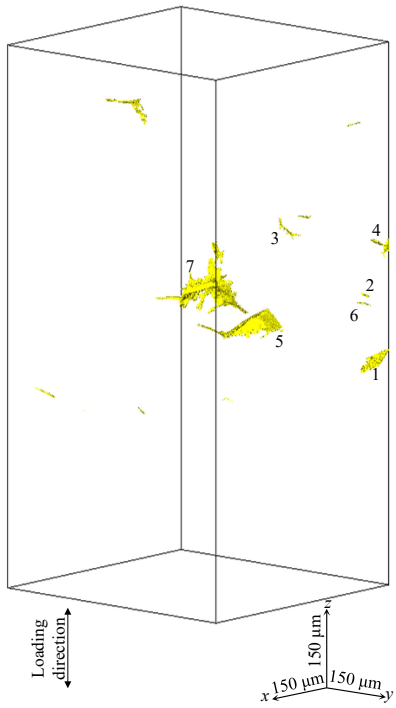

Fig. 3 3D cracks image at $\varepsilon_{appl} = 3.2\%$. The numbers in the figure represent the crack IDs of the cracks in the region of interest.

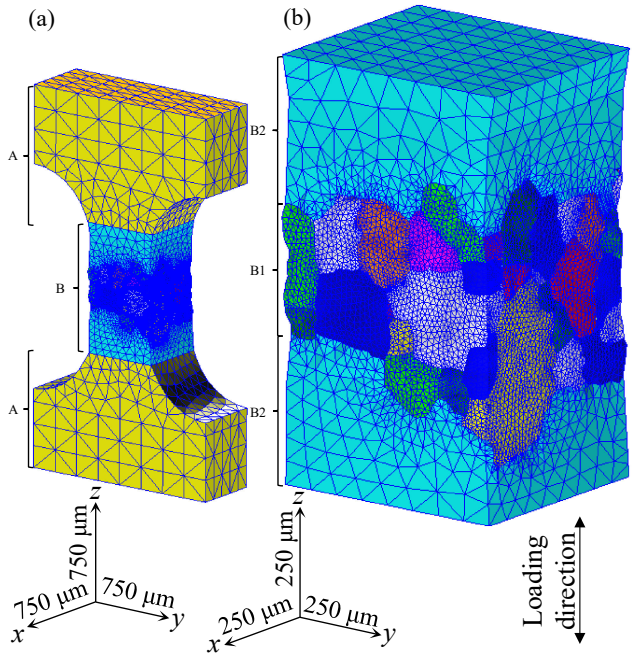

Fig. 4 3D image-based model. (a) whole view, (b) enlarged view of region B (B1 & B2).

localization and concentration was more pronounced than that of other GBs. The maximum hydrostatic stress value was 4.4×10^2 MPa, which was 3.7 times the overall average. The highest value of H concentration calculated by H diffusion analysis was 8.4 mass ppm, which was 1.2 times the initial H concentration.

Figure 6 shows the image of crack 4 and the distributions of hydrostatic stress and H concentration at $\varepsilon_{appl} = 0.97\%$ around the GB where crack 4 initiated. Localization of hydrostatic stress occurred at GB 1 and H concentration is higher than that of the surrounding area, suggesting that increased stress and H concentration due to crystal plasticity at the stage of $\varepsilon_{appl} = 0.97\%$ affected the initiation of crack 4. Among the surfaces, the hydrostatic stress is particularly high at the GB and plastic deformation is concentrated.

3.3 The relationship between stress concentration, H accumulation due to crystal plasticity and crack initiation behavior

From the results of CPFEM, equivalent plastic strain,

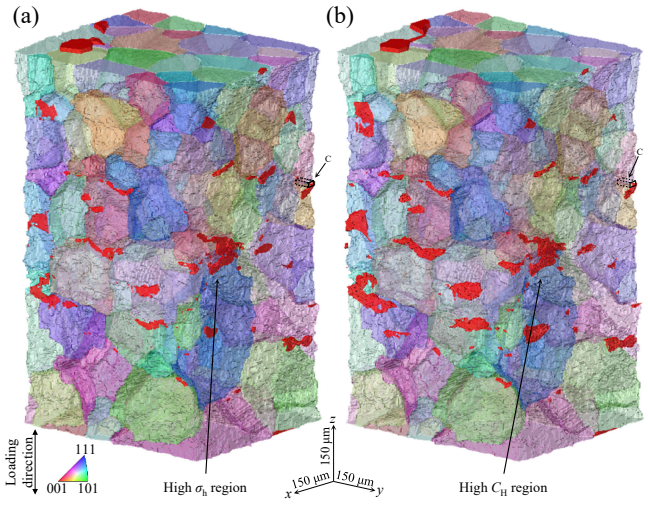

Fig. 5 (a) Hydrostatic stress distribution and (b) hydrogen concentration distribution superposed on the grains image at $\varepsilon_{appl} = 0.97\%$. Red regions represent the regions where (a) hydrostatic stress is larger than 133 MPa and (b) hydrogen concentration is larger than 7.08 mass ppm. The areas enclosed by the black border represent region C, where crack 4 occurred.

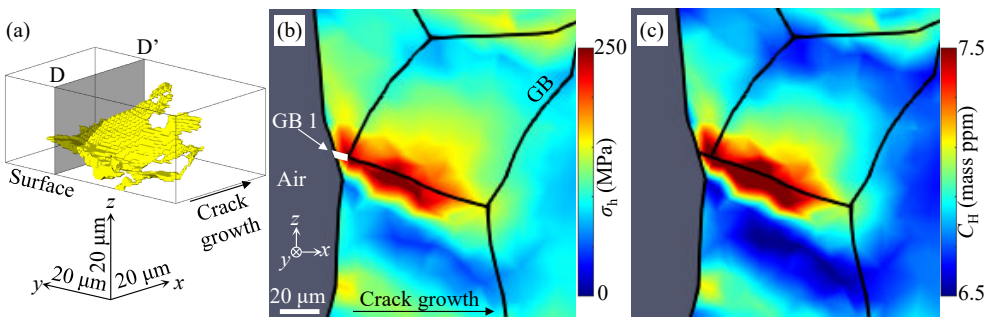

Fig. 6 (a) Image of crack 4 in the region C at $\varepsilon_{appl} = 3.2\%$ and distribution of (b) hydrostatic stress and (c) hydrogen concentration at slice DD′ around the GB where crack 4 initiated at $\varepsilon_{appl} = 0.97\%$. GB 1 (white line) is the GB where crack 4 occurred.

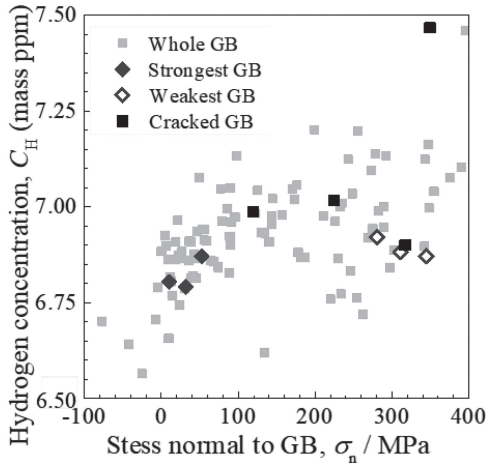

Fig. 7 Hydrogen concentration and stress normal to grain boundary (GB) of GBs where is in the region of interest at $\varepsilon_{appl} = 0.97\%$. Cracked GB represents the GBs where initial cracks originated from GB, not triple junction. Weakest GB represents the top 3 GBs with GB properties close to the weakest GB described in previous study [35]. Strongest GB represents the top 3 GBs with GB properties close to the strongest GB described in previous study [35].

hydrostatic stress, strain normal to GB, and stress normal to GB were calculated. These values were compared between GBs with and without initiation of initial cracks. Comparisons were also made between GB triple lines with and without initiation of initial cracks. It was found that stress normal to GB was most correlated with initiation of initial cracks. For GB on the specimen surface within the region of interest, the H concentration and the stress normal to GB at each node were averaged within the GB and plotted for each GB as shown in Fig. 7. The stress normal to GB tended to be higher at the GB where initial cracking occurred. However, there was no clear relationship between initiation of initial cracks and H concentration. For the GB triple line, no relationship with initiation of initial cracks was observed for the values of equivalent plastic strain, hydrostatic stress, strain normal to GB, and stress normal to GB.

4. Discussion

4.1 The effect of H accumulation on GB on crack initiation

Crack initiation is considered to be caused by H concentration on the GB, which leads to strength loss and high stress loading. Therefore, we discuss the crack initiation behavior in terms of both H concentration and mechanical factors. As for the H concentration, no clear relationship was found between the H concentration on the GB and crack initiation. This is contrary to the expectation that crack initiation is caused by H concentration due to interactions between grains. This can indicate the existence of a different mechanism of intergranular fracture than the separation of GB itself due to H concentration on the GB. HE fracture inside grain in Al-Zn-Mg alloys can originate from interfacial decohesion due to H segregation at the coherent or semi-coherent interface of precipitates inside grains [19, 30]. Since precipitates also exist on GBs in Al-Zn-Mg alloys, intergranular fractures may originate from interfacial decohesion of precipitate rather than the GBs. According to Gronsky *et al.*, GB precipitates in Al-Zn-Mg alloys have at least one coherent or semi-coherent interface with the grain [31]. Moreover, the maximum binding energy between the GB and H is 0.25 eV [10], while that of the coherent and semi-coherent interfaces of the precipitates are 0.35 eV [32] and 0.55 eV [19], respectively. Thus, the H concentration at the GB precipitate interface is expected to be higher than that at the GB. In this case, the H trapping behavior at the precipitate interface is expected to affect crack initiation behavior. H trapping at the precipitate interface is also governed by factors other than interactions between the grains, such as precipitate size, distribution, and interfacial coherence. Therefore, if H trapping at precipitate interfaces affects the crack initiation behavior, the effect of H enrichment due to interactions between the grains does not need to be large. According to Park *et al.*, GB precipitates in T73-tempered 7075 alloy have at least one semi-coherent interface with the grain [33]. In the material used in our study, the intergranular precipitates are considered to have semi-coherent interfaces because the temper is equivalent to T73. Therefore, H trapping at the precipitate interface is expected to influence crack initiation behavior, reducing the effect of H enrichment caused by interactions between the grains. This would be a reason why the correlation between the H concentration calculated and crack initiation behavior at GBs was not observed. In addition, as discussed in section 2.1, the composition and aging conditions of the specimens used in this study are considered to be sufficient for the material to be affected by HE. Therefore, the result that the correlation between H enrichment, which is caused by the interaction between the grains and crack initiation behavior is low is considered to occur under the condition that fracture of material is affected by HE.

Another reason for the lack of a clear relationship between H concentration on the GB and crack initiation behavior could be another factor that would increase the whole H concentration even more than estimation in the present study. The H diffusion analysis considered only internal H diffusion. Therefore, H ingress from the external environment was not considered in this study. If penetration of external H occurs, the actual H concentration would be higher than the value calculated in the H diffusion analysis. Although it is difficult to quantify the increase in H concentration due to external H ingress, some attempts have been made to indirectly evaluate external H ingress by calculating the fugacity of the external H. For example, Young *et al.* found that the fugacity of external H reaches 10^{67} Pa under a humid environment [34]. Therefore, even under normal atmospheric conditions, H can penetrate from the outside due to the high fugacity. The amount of internal H concentration calculated in our study is at most 1.2 times that of the unloading condition, which can be small compared to the amount of concentration due to external H ingress. In the future, it will be necessary to control the presence or absence of external H ingress, and to take a separate approach for the effects of internal and external H.

4.2 The effect of stress normal to GB on crack initiation behavior

Regarding the mechanical factor, there was a tendency for

initiation of initial cracks at GB with high stress normal to GB, but it was not a strong tendency. This can be because the evaluation was performed using a small number of cracks, 4. Toda *et al.* applied a statistical method to the evaluation of initiation behavior of 41 intergranular cracks to clarify the correlation between crystallographic factors and HE crack initiation in a pure ternary Al-Zn-Mg alloy (10 mass% Zn, 1.1 mass% Mg) [35]. The high correlation coefficients between GB area and GB orientation angle against the normal to the tensile direction were 0.12 and 0.23. Additionally, it was reported that the GB with smaller areas and orientation angles are more likely to crack. In the study, it was reported that the values of area and orientation angle of the weakest GB, which is estimated to be the most susceptible to crack initiation were $5.6 \times 10^3\,\mu m^2$ (average of all GB is $1.8 \times 10^4\,\mu m^2$) and 16.2° (average of all GB is 48.0°), respectively [35]. From the data in the present study, three GBs with values closest to those values were extracted and plotted in Fig. 7. The three GBs with the smallest value of E calculated by eq. (9) were selected as the three GB to be extracted.

$$E = (x - x_i)^2 + (y - y_i)^2 \tag{9}$$

Here, x and y are the normalized values of the area and orientation angle of the weakest GB determined by Toda *et al.*, and x_i and y_i are the values of the area and orientation angle of each GB in the present study, respectively. In addition, three other GBs were extracted and plotted in the same way for the GB that were estimated by Toda *et al.* to be the most unlikely to cause cracks (the strongest GB) [35]. The values of area and orientation angle of the strongest GB determined by Toda *et al.* are $5.1 \times 10^4\,\mu m^2$ and 88.4°, respectively [35]. The normal stress is higher at the weakest GB, and weak at the strongest GB. This means that GB with small area and orientation angle tend to have high normal stress normal and such a GB are prone to crack initiation. Therefore, the normal stress is considered to be the dominant mechanical factor for crack initiation. However, Fig. 7 shows that the plots of the three GB considered as the weakest GB do not coincide with the plots of the four GB where initial crack initiated. This may be because the three weakest GB were determined based only on the parameters of area and orientation angle, although GB precipitates and external H may also influence crack initiation, as described in section 4.1. Such factors may have increased the susceptibility to crack initiation at GB different from the three weakest GB plotted in Fig. 7, and crack initiation may have occurred on these GB. However, the trend of high normal stress at the cracked GB is consistent with the trend of high stress normal to GB at the weakest GB. Therefore, it is at least certain that the stress normal to GB is the dominant factor in crack initiation.

The above suggests that H enrichment due to internal H diffusion and external H intrusion reduces the strength of the GB precipitate interface, and high stress normal to GB is applied there, causing initiation of intergranular cracks.

5. Conclusion

Multi-modal 3D image-based simulation were performed to analyze the effect of crystal plasticity on the initiation of intergranular cracks in Al-8.4%Zn-0.99%Mg. As a result, the following findings were obtained in terms of H concentration and mechanical factors.

No clear relationship was found between the H concentration and crack initiation behavior. This may be because the influence of H trapping in GB precipitates and the intrusion of external H on crack initiation were not considered and only the concentration at GBs of internal H due to crystal plasticity was considered. In addition, the GB with higher stress normal to GB tended to be more prone to initiation of initial cracks. The stress normal to GB, which is increased by crystal plasticity, is considered to be the dominant mechanical factor in crack initiation. From these considerations, it is considered that the strength of the GB precipitate interface is reduced by H enrichment due to internal H diffusion and external H intrusion, and that the initiation of intergranular cracks is caused by the high stress normal to GB because of crystal plasticity.

Acknowledgments

This work was funded by JST CREST “Nano Mechanics” (JPMJCR1995), and JSPS KAKENHI (JP20J11740), and supported by a grant from the Light Metal Educational Foundation. The synchrotron radiation experiments were carried out under SPring-8 proposals (2018A0076). The authors used Information and Media Center in Toyohashi University of Technology for the CPFEM and thank to Mr. Soma Ito, Mr. Reiki Ishikawa and Mr. Shogo Furuta for contributing to the CPFEM analysis.

REFERENCES

[1] S.J. Won, H. So, L. Kang, S.J. Oh and K.H. Kim: Development of a high-strength Al-Zn-Mg-Cu-based alloy via multi-strengthening mechanisms, Scr. Mater. **205** (2021) 114216.

[2] Y. Xu, Z. Zhang, Z. Gao, Y. Bai, P. Zhao and W. Mao: Effect of main elements (Zn, Mg and Cu) on the microstructure, castability and mechanical properties of 7xxx series aluminum alloys with Zr and Sc, Mater. Charact. **182** (2021) 111559.

[3] D. Yuan, S. Chen, K. Chen, L. Huang, J. Chang, L. Zhou and Y. Ding: Correlations among stress corrosion cracking, grain-boundary microchemistry, and Zn content in high Zn-containing Al-Zn-Mg-Cu alloys, T. Nonferr. Metal Soc. **31** (2021) 2220–2231.

[4] C. Altenbach, C. Schnatterer, U.A. Mercado, J.P. Suuronen, D. Zander and G. Requena: Synchrotron-based holotomography and X-ray fluorescence study on the stress corrosion cracking behavior of the peak-aged 7075 aluminum alloy, J. Alloy. Compd. **817** (2020) 152722.

[5] L. Oger, E. Andrieu, G. Odemer, L. Peguet and C. Blanc: About the role of the hydrogen during stress corrosion cracking of a low-copper Al-Zn-Mg alloy, J. Alloy. Compd. **900** (2022) 163391.

[6] E. Schwarzenböck, L. Wiehler, T. Heidenblut, T. Hack, C. Engel and H.J. Maier: Crack initiation of an industrial 7XXX aluminum alloy in humid air analyzed via slow strain rate testing and constant displacement testing, Mater. Sci. Eng. A **804** (2021) 140776.

[7] U.D. Francisco, F. Beckmann, J. Moosmann, N.O. Larrosa and M.J. Peel: 3D characterisation of hydrogen environmentally assisted cracking during static loading of AA7449-T7651, Int. J. Fract. **232** (2021) 93–116.

[8] Y. Aboura, A.J. Garner, R. Euesden, Z. Barrett, C. Engel, N.J.H. Holroyd, P.B. Prangnell and T.L. Burnett: Understanding the environmentally assisted cracking (EAC) initiation and propagation of new generation 7xxx alloys using slow strain rate testing, Corros. Sci. **199** (2022) 110161.

[9] R.A. Oriani and P.H. Josephic: Equilibrium aspects of hydrogen-induced cracking of steels, Acta Metall. **22** (1974) 1065–1074.
[10] M. Yamaguchi, K. Ebihara, M. Itakura, T. Tsuru, K. Matsuda and H. Toda: First-principles calculation of multiple hydrogen segregation along aluminum grain boundaries, Comput. Mater. Sci. **156** (2019) 368–375.
[11] R. Miresmaeili, N. Saintier, H. Notsu, J.M. Olive and H. Kanayama: One-Way Coupled Crystal Plasticity-Hydrogen Diffusion Simulation on Artificial Microstructure, J. Comput. Sci. Technol. **4** (2010) 105–120.
[12] A. Arora, R. Kumar, H. Singh and D.K. Mahajan: Hydrogen assisted crack initiation in metals under monotonic loading: A new experimental approach, Theor. Appl. Fract. Mech. **112** (2021) 102917.
[13] E. Pouillier, A.F. Gourgues, D. Tanguy and E.P. Busso: A study of intergranular fracture in an aluminium alloy due to hydrogen embrittlement, Int. J. Plast. **34** (2012) 139–153.
[14] A. Zeghadi, S. Forest, A.F. Gourgues and O. Bouaziz: Ensemble averaging stress–strain fields in polycrystalline aggregates with a constrained surface microstructure – Part 2: crystal plasticity, Philos. Mag. **87** (2007) 1425–1446.
[15] A.C. Lewis and A.B. Geltmacher: Image-based modeling of the response of experimental 3D microstructures to mechanical loading, Scr. Mater. **55** (2006) 81–85.
[16] H. Proudhon, J. Li, P. Reischig, N. Gueninchault, S. Forest and W. Ludwig: Coupling Diffraction Contrast Tomography with the Finite Element Method, Adv. Eng. Mater. **18** (2016) 903–912.
[17] H. Fujihara, H. Toda, K. Ebihara, M. Kobayashi, T. Mayama, K. Hirayama, K. Shimizu, A. Takeuchi and M. Uesugi: Assessment of hydrogen embrittlement behavior in Al-Zn-Mg alloy through multi-modal 3D image-based simulation, Int. J. Plast. **174** (2024) 103897.
[18] K. Shimizu, H. Toda, K. Uesugi and A. Takeuchi: Local Deformation and Fracture Behavior of High-Strength Aluminum Alloys Under Hydrogen Influence, Metall. Mater. Trans. A **51** (2020) 1–19.
[19] K. Shimizu, H. Toda, K. Hirayama, H. Fujihara, T. Tsuru, M. Yamaguchi, A. Bendo, K. Matsuda, M. Uesugi and A. Takeuchi: Acta Mater., to be submitted.
[20] M.S. Bhuiyan, H. Toda, K. Uesugi, A. Takeuchi and Y. Watanabe: Damage micromechanisms in high Mn and Zn content 7XXX aluminum alloys, Mater. Sci. Eng. A **793** (2020) 139423.
[21] G.A. Young and J.R. Scully: Hydro. Effec. Mater. Behav. Corros. Defor. Inter. (2003) 893–907.
[22] A.C. Kak and M. Slaney: *Principles of Computerized Tomographic Imaging*, (Soc. Ind. Appl. Math., Philadelphia, 2001).
[23] Y. Huang: A User-Material Subroutine Incorporating Single Crystal Plasticity in the ABAQUS Finite Element Program, Harvard Univ., (1991).
[24] J.W. Hutchinson: Bounds and self-consistent estimates for creep of polycrystalline materials, Proc. R. Soc. London Ser. A **348** (1976) 101–127.
[25] J. Pan and J.R. Rice: Rate sensitivity of plastic flow and implications for yield-surface vertices, Int. J. Solids Struct. **19** (1983) 973–987.
[26] D. Peirce, R.J. Asaro and A. Needleman: Material rate dependence and localized deformation in crystalline solids, Acta Metall. **31** (1983) 1951–1976.
[27] Y. Zhou, K.W. Neale and L.S. Toth: A modified model for simulating latent hardening during the plastic deformation of rate-dependent FCC polycrystals, Int. J. Plast. **9** (1993) 961–978.
[28] R.A. Oriani: The diffusion and trapping of hydrogen in steel, Acta Metall. **18** (1970) 147–157.
[29] M.S. Bhuiyan, Y. Tada, H. Toda, S. Hang, K. Uesugi, A. Takeuchi, N. Sakaguchi and Y. Watanabe: Influences of hydrogen on deformation and fracture behaviors of high Zn 7XXX aluminum alloys, Int. J. Fract. **200** (2016) 13–29.
[30] T. Tsuru, K. Shimizu, M. Yamaguchi, M. Itakura, K. Ebihara, A. Bendo, K. Matsuda and H. Toda: Hydrogen-accelerated spontaneous microcracking in high-strength aluminium alloys, Sci. Rep. **10** (2020) 1998.
[31] R. Gronsky and P. Furrer: Grain boundary precipitation in aluminum alloys: Effect of boundary structure, Metall. Trans. A **12** (1981) 121–127.
[32] T. Tsuru, M. Yamaguchi, K. Ebihara, M. Itakura, Y. Shiihara, K. Matsuda and H. Toda: First-principles study of hydrogen segregation at the $MgZn_2$ precipitate in Al-Mg-Zn alloys, Comput. Mater. Sci. **148** (2018) 301–306.
[33] J.K. Park and A.J. Ardell: Precipitation at grain boundaries in the commercial alloy Al 7075, Acta Metall. **34** (1986) 2399–2409.
[34] G.A. Young and J.R. Scully: The effects of test temperature, temper, and alloyed copper on the hydrogen-controlled crack growth rate of an Al-Zn-Mg-(Cu) alloy, Metall. Mater. Trans. A **33** (2002) 1167–1181.
[35] H. Toda, K. Hirayama, S. Yamaguchi, H. Fujihara, R. Higa, K. Shimizu, A. Takeuchi and M. Uesugi: Dominant Factors Controlling the Initiation of Hydrogen Embrittlement in Al–Zn–Mg Alloy, Mater. Trans. **64** (2023) 2729–2738.